

# Aspects regarding measurement of thickness of intergranular glassy films

S. BHATTACHARYYA, A. SUBRAMANIAM, C. T. KOCH & M. RÜHLE

Max-Planck-Institut für Metallforschung, Stuttgart, Germany

**Key words.** Fourier filtering, Fresnel fringes, high-resolution electron microscopy, intergranular glassy film,  $\text{Si}_3\text{N}_4$ ,  $\text{SrTiO}_3$ .

## Summary

Materials such as  $\text{Si}_3\text{N}_4$ ,  $\text{SiC}$  and  $\text{SrTiO}_3$  can have grain boundaries characterized by the presence of a thin intergranular amorphous film of nearly constant thickness, in some cases (e.g.  $\text{Si}_3\text{N}_4$ ) almost independent of the orientation of the bounding grains, but dependent on the composition of the ceramic. Microscopy techniques such as high-resolution lattice fringe imaging, Fresnel fringe imaging and diffuse dark field imaging have been applied to the study of intergranular glassy films. The theme of the current investigation is the use of Fresnel fringes and Fourier filtering for the measurement of the thickness of intergranular glassy films. Fresnel fringes hidden in high-resolution micrographs can be used to objectively demarcate the glass–crystal interface and to measure the thickness of intergranular glassy films. Image line profiles obtained from Fourier filtering the high-resolution micrographs can yield better estimates of the thickness. Using image simulation, various kinds of deviation from an ideal square-well potential profile and their effects on the Fresnel image contrast are considered. A method is also put forth to objectively retrieve Fresnel fringe spacing data by Fourier filtering Fresnel contrast images. Difficulties arising from the use of the standard Fresnel fringe extrapolation technique are outlined and an alternative method for the measurement of the thickness of intergranular glassy films, based on zero-defocus (in-focus) Fresnel contrast images is suggested. The experimental work is from two ceramic systems: Lu-Mg-doped  $\text{Si}_3\text{N}_4$  and  $\text{SrTiO}_3$  (stoichiometric and nonstoichiometric). Further, a comparison is made between the standard high-resolution lattice fringe technique, the standard Fresnel fringe extrapolation technique and the methods of analyses introduced in the current work, to illustrate their utility and merits. Taking experimental difficulties into account, this work is intended to be a practical tool kit for the study of intergranular glassy films.

## Introduction

Intensive research in the last few decades has given considerable insight into the structure of interfaces in materials, such as  $\text{Si}_3\text{N}_4$  and  $\text{SiC}$ , that have an equilibrium thickness intergranular glassy film (IGF) (Kleebe, 1992; Kleebe, 1997). Various electron microscopic techniques have been applied to the study of IGFs and these investigations have yielded important information regarding the structure of these films and their interface with the bounding grains. These techniques include, high-resolution electron microscopy (Cinibulk *et al.*, 1993), Fresnel fringe imaging (Rasmussen & Carter, 1990), diffuse dark field imaging (Cinibulk *et al.*, 1993), energy-filtered electron diffraction (Koch *et al.*, 2004), high-angle annular dark field scanning transmission electron microscopy (Shibata *et al.*, 2004; Winkelman *et al.*, 2005) and holography (Elfving & Olsson, 2002). Comparative analyses of these techniques have been carried out at various times and the works of Simpson *et al.* (1986), Cinibulk *et al.* (1993), Kleebe (1997) and MacLaren (2004) are noteworthy. High-resolution lattice fringe imaging has been cited as the most reliable technique for the reproducible measurement of the thickness of IGFs (Cinibulk *et al.*, 1993).

In the Fresnel fringe-imaging technique, the thickness of the IGF can be obtained by extrapolation of the fringe spacing data (Clarke, 1979; Jin *et al.*, 1998), Ness *et al.* (1986), Rasmussen & Carter (1990), Ross & Stobbs (1991), Dunin-Borkowski (2000) and Loudon *et al.* (2001) have used Fresnel imaging through focal series data to obtain the potential profile across grain boundaries (GBs). Further, holographic methods, such as off-axis (Elfving & Olsson, 2002; Wang & Dravid, 2002) or in-line holography (Bhattacharyya *et al.*, 2006) retrieve the exit face wave function and yield the projected potential profile across GBs.

Earlier models (Ackler, 1997; Bobeth *et al.*, 1999) and recent work (Shibata *et al.*, 2004; Ziegler *et al.*, 2004) have shown that the interface between the IGF and the bounding crystal is not abrupt but diffuse. This is also reflected in the high-resolution micrographs (HRMs) (Döblinger *et al.*, 2004). This poses important questions as to how a given technique can be

optimally used for the measurement of the thickness of an IGF and how meaningful comparisons with results from other techniques can be made.

In the study of IGFs by high-resolution microscopy, there are often constraints imposed either by the material or by the microscope. In some materials (e.g. stoichiometric SrTiO<sub>3</sub>), the frequency of GBs with an IGF is very small. In samples with large grain size (~tens of microns), only very few interfaces may be observed within the thin region of the sample, making this problem even more severe. Hence maximum use of GBs with an IGF should be made for measurements. In SrTiO<sub>3</sub> samples (used for this study) the grain boundaries were usually not planar and only a portion of the GB could be aligned approximately edge-on. This implies that tilt along an axis perpendicular to the GB (i.e. keeping the boundary edge-on) is severely limited. Microscope-imposed constraints are mainly related to resolution and available tilt angles. For SrTiO<sub>3</sub>, only five planes fall into the resolution range of a standard microscope such as a JEOL 4000EX (JEOL Ltd., Tokyo, Japan) [(001) (101) (111) (002) and (102)]. In this microscope, with a top entry holder, the tilt available is  $\pm 10^\circ$  and sharp lattice fringe contrast could sometimes not be obtained on both sides of the IGF within this tilt regime.

The Fresnel fringe extrapolation technique, in spite of its utility, suffers from its own set of limitations imposed by the microscope or material used. Various sources of noise add to uncertainty in the measurements, especially at low defocus values (Williams & Carter, 1996). Lower accelerating voltage microscopes (e.g. Zeiss-912, 120 kV, Carl Zeiss AG, Germany) are preferred for certain investigations, wherein electron beam-induced knock-on damage needs to be minimized. Due to an in-column energy filter (used to stop the inelastically scattered electrons), the Zeiss-912 has the advantage that it gives excellent Fresnel contrast images (FCIs), but the region of defocus values giving interpretable Fresnel contrast is limited (~1–3  $\mu\text{m}$ ). As the source of Fresnel contrast is the difference in potential across the interface, a small potential difference can lead to poor contrast. While differences in the projected potential of grain and IGF may be intrinsic local material properties, we need to keep in mind that the projected potential is also affected by surface grooving due to the preferential etching of either material during specimen preparation. In the standard Fresnel imaging technique, a square-well potential is assumed across the GB. Under these assumptions, the Fresnel intensity profile for a given value of underfocus is related to the profile for the corresponding overfocus by a mirror inversion with respect to zero defocus (Ness *et al.*, 1986). This perfect symmetry has been found to be absent in real boundaries with an IGF and hence the analysis needs to be modified. Additionally, for diffuse interfaces, the contrast decreases rapidly as the defocus value approaches zero (Rasmussen & Carter, 1990). This implies that best use of the available images is required to avoid large errors possibly being introduced in the usual method of extrapolation of the data.

In the present work, the following tasks were attempted:

- (i) Measuring the thickness of an IGF objectively from Fresnel fringes hidden in high-resolution micrographs and also enhancing the utility of HRMs with weak lattice fringe contrast.
- (ii) Fourier filtering (FF) of Fresnel images for contrast enhancement and for (a) measuring the thickness of IGFs and (b) finding the zero-defocus (in-focus) condition.
- (iii) Addressing issues related to the calculation of the thickness of an IGF using the Fresnel fringe spacing extrapolation technique (simulation and experiments).
- (iv) Understanding the different kinds of deviation from an ideal square-well potential in terms of their effect on the Fresnel contrast profiles (by simulation).
- (v) Measuring the thickness of IGFs from a zero-defocus FCI (noting that the contrast observed at zero-defocus is not the classical Fresnel contrast).

The methodologies developed will be tested on experimental images of Lu-Mg-doped Si<sub>3</sub>N<sub>4</sub> (henceforth referred to as the 'Si<sub>3</sub>N<sub>4</sub> sample') and SrTiO<sub>3</sub> (stoichiometric and nonstoichiometric SrTiO<sub>3</sub>) samples. Si<sub>3</sub>N<sub>4</sub> and SrTiO<sub>3</sub> represent vastly different cases, when it comes to processing routes, grain size, frequency of occurrence of IGFs, faceting of the grains and the 'straightness' of the GB.

A comparison of the thickness obtained by the different methods will be made. The emphasis will be on the optimum use of recorded data, which reflect the real experimental conditions.

## Materials and methods

Dense silicon nitride samples were prepared from milled and sieved  $\alpha$ -Si<sub>3</sub>N<sub>4</sub> (88.07 wt%), SiO<sub>2</sub> (2.16 wt%), MgO (1.07 wt%) and Lu<sub>2</sub>O<sub>3</sub> (8.7 wt%) powders, by first cold pressing, then sintering at 1750 °C for 15 min at a pressure of 10 bar and finally hot isostatic pressing at 1750 °C for 60 min at 100 bar (Satet & Hoffmann, 2004).

SrTiO<sub>3</sub> samples were prepared by mixing SrCO<sub>3</sub> and TiO<sub>2</sub> in two compositions: (i) stoichiometric (TiO<sub>2</sub>/SrCO<sub>3</sub> = 1/1) and (ii) nonstoichiometric (TiO<sub>2</sub>/SrCO<sub>3</sub> = 1/0.98) and calcined in two stages (calcination 1 : 18 h, 975 °C; calcination 2 : 15 h, 1050 °C). During calcination the heating rate was 20 °C min<sup>-1</sup> and the cooling rate was 10 °C min<sup>-1</sup>. The powders were sintered by the following steps: (i) heating in air at 1340 °C for 6 h; (ii) hot isostatically pressed at 1300 °C and  $2 \times 10^7$  Pa in an Argon atmosphere; and (iii) heated at 1480 °C for 3 h in air to reach a higher density. The stoichiometric composition was designated STO1 and the nonstoichiometric composition STO2. The Si<sub>3</sub>N<sub>4</sub> and SrTiO<sub>3</sub> samples were provided by Dr Raphaele Satet and Prof. Michael Hoffmann of the University of Karlsruhe.

Specimens for transmission electron microscopy were prepared by the standard techniques of grinding, dimpling and ion-beam thinning (Precision Ion Polishing System, Gatan Inc., Pleasanton,

CA, U.S.A.). The ion-beam thinning was carried out at an angle of inclination of  $8^\circ$  of the ion beam to the sample. The  $\text{Si}_3\text{N}_4$  specimens were coated with a thin layer of carbon to minimize charging under the electron beam.

Three transmission electron microscopes were used. These were: (i) a JEOL 4000 FX; (ii) a JEOL JEM 4000 EX; and (iii) a Zeiss-912. The JEOL 4000 FX (point-to-point resolution 0.2 nm), operated at 400 kV was used for examining the  $\text{Lu}_2\text{O}_3$ -MgO-doped  $\text{Si}_3\text{N}_4$  specimen. Images were taken on Kodak electron image film (SO-163) (Eastman Kodak Co., Rochester, New York) at a magnification of 500 000 $\times$ . The JEOL JEM 4000 EX (operated at 400 kV), dedicated to high resolution performance (point-to-point resolution 0.18 nm), was used for examining the  $\text{SrTiO}_3$  samples. In this microscope, the magnification and films (for recording images) are identical to those in the JEOL 4000 FX. The Zeiss-912 microscope (LaB<sub>6</sub>, Köhler illumination), operated at 120 kV and equipped with an in-column energy filter, was also used for examining the  $\text{Lu}_2\text{O}_3$ -MgO-doped  $\text{Si}_3\text{N}_4$  specimen. Experiments with the Zeiss-912 were carried out using an electron beam convergence semiangle ( $\theta_c$ ) of 1.0 mrad.

Using the Zeiss-912 microscope energy-filtered images were obtained using a 15 eV energy window centred on the zero loss peak. The images were captured onto a  $1024 \times 1024$  pixel charge-coupled device (CCD) array at a sampling density relative to the specimen of 0.19 nm per pixel (images were taken at a magnification of 80 000 $\times$ ). A series of images (through focal series) was acquired in the defocus range of 1 to 2.2  $\mu\text{m}$  with a step size of 0.2  $\mu\text{m}$  in both over- and underfocus conditions. Additionally, images at and close to zero-defocus were also obtained.

For these experiments, the boundaries of interest were tilted to orientate them parallel to the incident electron beam (edge-on condition). For lattice and Fresnel fringe imaging, the specimen was further tilted, keeping the grain boundary parallel to the electron beam, using procedures described by Cinibulk *et al.* (1993) and Stobbs & Ross (1989), respectively.

Clarke's (1979) standard method was used to measure the thickness from high-resolution micrographs (using lattice fringe imaging) in addition to the methods developed in the current work. The Fresnel fringe techniques developed in the present

investigation were compared with the standard Fresnel fringe extrapolation method (Clarke, 1979; Cinibulk *et al.*, 1993; Jin *et al.*, 1998). In the conventional Fresnel extrapolation method for measuring the thickness of IGFs, fringe spacing values ( $s$ ) have been plotted as a function of defocus ( $\Delta f$ ) (Jin *et al.*, 1998). Jin *et al.* (1998) used the following equation relating fringe spacing ( $s$ ) to IGF thickness ( $s_0$ ) and defocus ( $\Delta f$ ):

$$s = s_0 + c\Delta f^{1/2} \quad (1)$$

where  $c$  is a microscope-dependent constant. This formula implies a linear plot of  $s$  versus  $\sqrt{\Delta f}$  and extrapolation to zero-defocus gives the thickness of the IGF.

Digital micrograph software (Gatan Inc.) was used to obtain line profiles across the interface from each of the digitized images (integrated over suitable widths; usually of 100 pixels) and also for Fourier filtering the experimental images. MATLAB-R12 software was used to implement the algorithms used in the simulations.

#### Fourier filtering

To illustrate the utility of the Fourier filtering method we consider an image with a diffuse contrast across the grain boundary with an IGF. Figure 1(a) shows the diffuse dark field image taken from the stoichiometric  $\text{SrTiO}_3$  sample and the intensity profile across the interface (inset). Measurement of the thickness from such an image could prove to be quite subjective, which makes comparison with other results difficult. Figure 1(b) shows the corresponding Fourier filtered image, obtained by masking the central spot in the Fourier transformation (FT), with a mask size of  $0.073 \text{ nm}^{-1}$  [the unmasked region is used for the inverse Fourier transformation (IFT)]. This is equivalent to subtracting a low-resolution (resolution = 13.7 nm) image from the original. The enhancement in contrast and ease of measurement of the thickness can be seen in Fig. 1. The use of this method for the case of the FCI is described next. In this work, the acronym FCI is also used for simulated Fresnel contrast profiles.

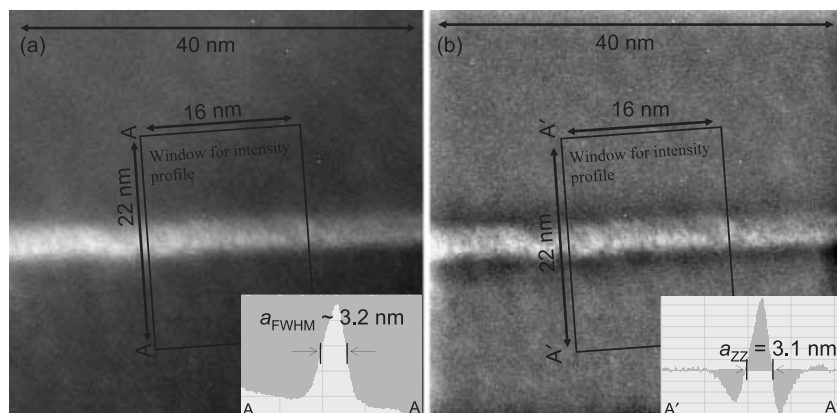


**Fig. 1.** Illustration of the difficulty in measuring widths from images with diffuse interface contrast. (a) Diffuse dark field image from a grain boundary in the stoichiometric  $\text{SrTiO}_3$  sample (STO1), with the plot of the profile across the image (line AA) shown in the inset. (b) Fourier-filtered image using a mask of  $0.073 \text{ nm}^{-1}$  diameter with the profile across A'A' as the inset.

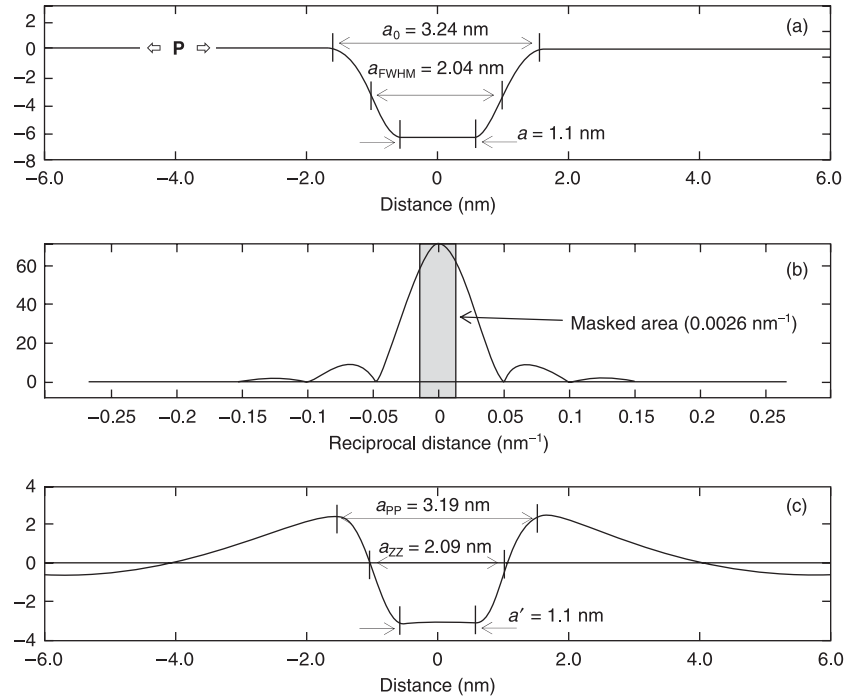


**Fig. 2.** Effect of Fourier filtering on a diffuse scattering potential profile. (a) The scattering potential; (b) the Fourier transformation of the profile with a superimposed mask [the shaded region is excluded in the inverse Fourier transformation (IFT)]; (c) the IFT after application of the mask. The various distances ( $a$ ,  $a_0$ ,  $a_{\text{FWHM}}$ ,  $a'$ ,  $a_{\text{ZZ}}$ ,  $a_{\text{PP}}$ ) are given in the images for reference.

**Table 1.** Parameters and assumptions used in the current simulations of Fresnel contrast images (FCIs) and Fourier-filtered (FF)-FCIs.

Parameter	Designation	Value/description
Weak phase object approximation	WPOA	$\sigma, t = 0.01 \text{ V}^{-1}$
Phase object approximation	POA	$\sigma, t = 0.1 \text{ V}^{-1}$
Potential profile	P	FWHM = 2.04 nm, Diffuse interface on both sides
	P1	$a = a_0 = a_{\text{FWHM}} = 2.04 \text{ nm}$ , square-well potential
	P2	$a_{\text{FWHM}} = 2.04 \text{ nm}$ , left-right (LR) asymmetric profile
	P3	$a_{\text{FWHM}}$ (of well) = 2.04 nm, $a_{\text{FWHM}}$ (of bump) = 0.45 nm to simulate segregation
Wavelength ( $\lambda$ )	L1	0.00335 nm
Spherical aberration (Cs)	C1	2.7 mm
Accelerating voltage	–	120 kV
Objective aperture size	A0	Diffuse aperture with $d_{\text{FWHM}} = 0.02496 \text{ nm}^{-1}$
Mask size	M1	0.0026 $\text{nm}^{-1}$ (diameter)
	M2	0.0032 $\text{nm}^{-1}$ (diameter)
	M3	Mask with diffuse edges $d_{\text{FWHM}} = 0.0026 \text{ nm}^{-1}$
Beam sampling size	–	0.023 nm
Simulation cell size	–	12.673 nm

$\sigma$ , interaction constant;  $t$ , specimen thickness; FWHM, full width at half the maximum.

The size of the Fourier mask is an important parameter in the procedure and how it was chosen in the current investigation is described below. A mask that is too small is not useful as only the unmasked region is kept. However, a mask that is too large will lead to mask-induced artefacts in the IFT. As a first approximation, the mask should be smaller than the streak produced by the IGF in the FT of the image. To simulate the effect of the mask, the scattering potential across the IGF was chosen as in Fig. 2(a). The various parameters and assumptions used in the simulations performed in the current work

are listed in Table 1. The profile (P) has two Gaussian functions (replacing the vertical sections of a square-well potential) to describe the diffuseness of the crystal–glass interface. The depth of the potential profile was chosen as that between  $\text{Si}_3\text{N}_4$  (17.4 V) and  $\text{SiO}_2$  (10.9 V) (Peng, 1999; Koch *et al.*, 2005). Figure 2(b) shows the FT of the profile in Fig. 2(a) along with the superimposed mask (Fig. 2b: the shaded region is excluded in the IFT). Figure 2(c) shows the IFT after the application of the mask. The size of the mask ( $0.0026 \text{ nm}^{-1}$ ) was chosen to produce low contrast in the flat region of the profile (i.e. in

**Table 2.** A comparison of the spacings measured from a simulated Fourier filtered profile, using a mask of two sizes, with that from the original profile. The variables are defined in Fig. 2.

Mask size (nm <sup>-1</sup> )	From the profile (nm)			From the Fourier-filtered profile (nm)		
	$a_0$	$a_{\text{FWHM}}$	$a$	$a_{\text{pp}}$	$a_{\text{ZZ}}$	$a'$
0.0026 (M1)	3.24	2.08	1.1	3.19	2.09	1.1
0.0032 (M2)	3.24	2.08	1.1	3.10	1.97	1.16

the 'a' section in Fig. 2a). A good correspondence between the values measured is seen in Fig. 2. Table 2 summarizes the data from Fig. 2 along with the measurements obtained for a mask of 0.0032 nm<sup>-1</sup> in size. Due to the long tail of the Gaussian function (Fig. 2a), the value  $a_0$  is measured at 99% of the intensity of the profile. Secondary oscillations, which can be seen in the zoomed-out version of Fig. 2(c), are due to the sharp nature of the mask interface and the presence of secondary minima in the FT of the profile P (Fig. 2b).

The scattering potential profile shown in Fig. 2(a) is a one-dimensional (1D) projected potential profile. It must be understood that this profile cannot distinguish between the various structural cases illustrated in Fig. 3. All the three profiles shown

in Fig. 3 would be captured in a 1D profile as having a diffuse interface.

The effect of Fourier filtering on the plot of a Fresnel contrast profile is shown in Fig. 4 (the simulation of Fresnel contrast will be dealt with in the next section). Figure 4(a) shows the Fresnel intensity profile calculated from the scattering potential profile considered in Fig. 2(a), at a defocus value of +2.2  $\mu\text{m}$ . Application of the Fourier mask (as in Fig. 2c) leads to the Fourier-filtered Fresnel intensity profile as in Fig. 4(b). A good correspondence is seen in the spacings measured from the Fourier-filtered profile with the original profile. The values measured are marked in the figure. However, if we start with a zero-defocus FCI (Fig. 4c) and apply the Fourier mask, then the full width at half the maximum (FWHM) of the projected potential well can be directly measured from the FF-FCI (Fig. 4d,e). Figure 4(d) shows the Fourier-filtered plot obtained from the complex exit face wave function and Fig. 4(e) shows the FF-FCI obtained from the absolute value of the exit face wave function. Figure 4(e) is expected to correspond to the experimental profile (experimental intensity,  $I = |\Psi|^2 = (\text{absolute value})^2$ ).

The secondary oscillations seen in Fig. 4(b) are expected to be less prominent in the case of a diffuse mask which would reduce secondary oscillations. For somewhat diffuse interfaces this implies a monotonic dependence of the mask size on the spacings measured from the Fourier-filtered profile. Hence,

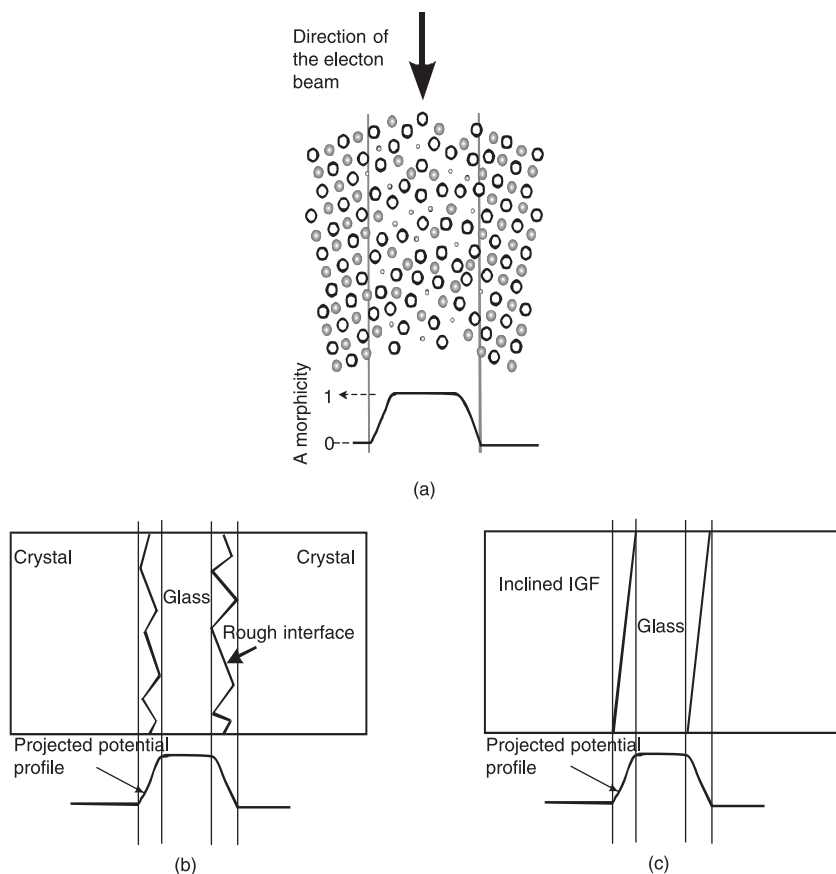


**Fig. 3.** Schematic illustration of the limitations of a one-dimensional projected potential profile, with respect to its ability to distinguish between various structural features in the grain boundary region having an intergranular glassy film. (a) Diffuse interface between glass and crystal; (b) rough interface; (c) inclined interface. All the three structures show a similar potential profile, as shown below each of the figures.

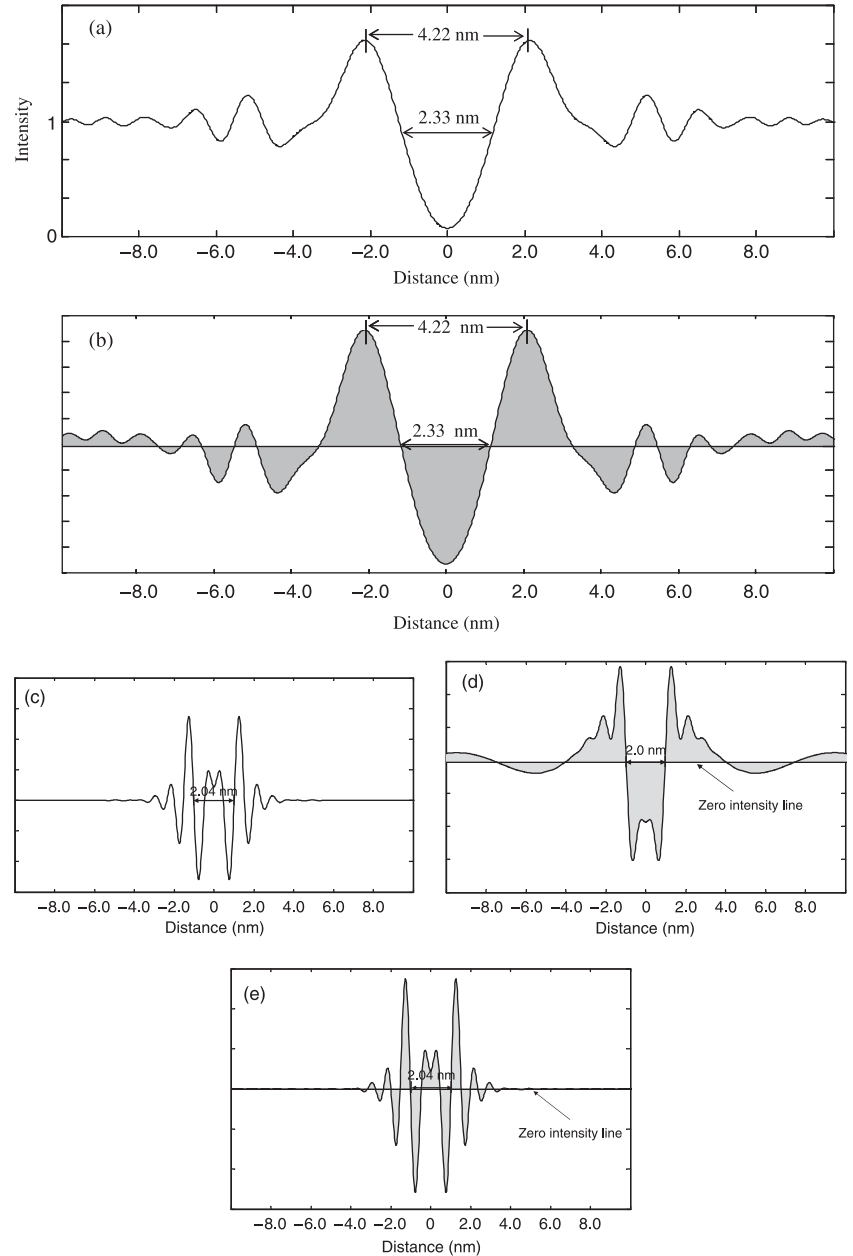


**Fig. 4.** The effect of Fourier filtering on a Fresnel contrast intensity profile. (a) Fresnel intensity profile calculated from the scattering potential considered in Fig. 2(a), at a defocus value of  $+2.2 \mu\text{m}$ ; (b) Fourier-filtered Fresnel intensity profile after application of the mask shown in Fig. 2(b) (M1); (c) Fresnel contrast image (FCI) at a defocus value of zero; (d) zero-defocus Fourier-filtered plot obtained from the complex exit phase wave function, using mask M1; (e) zero-defocus Fourier-filtered-FCI obtained from the absolute value of the exit phase wave function. The simulation parameters are: WPOA, C1, L1, A0 and M1 (see Table 1 for definitions of these).

the technique is expected to be reasonably robust with respect to mask size, for measurements from real FCIs. An additional point regarding the use of Fourier masking will be made in the next section.

### Potential profiles and Fresnel contrast

Using the phase-object approximation, the following equation (Spence, 1981) is used to simulate Fresnel profiles from one-dimensional potential profiles:

$$I_{(r)} = |FT^{-1}[FT(e^{-i\sigma V_{(r)}t})f_{\text{ap}}(k)e^{i\chi(k)}]|^2 \quad (2)$$

where  $I_{(r)}$  is the image intensity,  $i = \sqrt{-1}$ ,  $V_{(r)}$  is the potential profile across the interface,  $\sigma$  is the interaction constant,  $t$  is the specimen thickness,  $f_{\text{ap}}(k)$  is the objective aperture function in reciprocal space,  $e^{i\chi(k)}$  is the microscope contrast transfer function and  $FT^{-1}$  denotes the inverse Fourier transform operation. Neglecting aberrations other than defocus and spherical aberration,  $\chi(k)$  is given by  $\chi(k) = \pi\Delta f\lambda k^2 + \frac{1}{2}\pi C_s\lambda^3 k^4$ , where  $k$  is the reciprocal space coordinate. The values of the parameters used in the simulation are listed in Table 1.

Figure 5(a) shows the square-well potential profile usually used as the potential profile across the IGF for the calculation

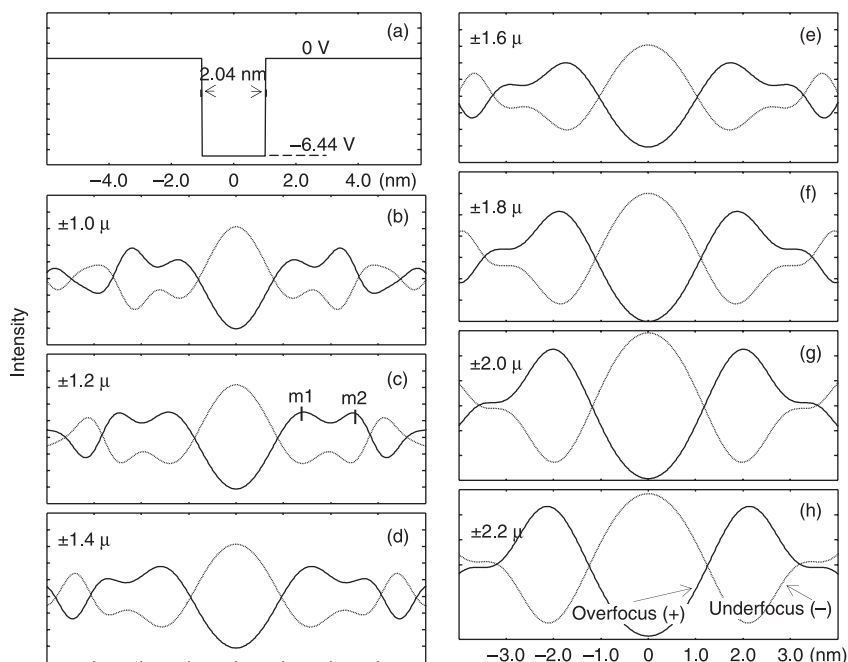


Fig. 5. (a) A square-well potential; (b–h) simulated Fresnel contrast plots for various over and underfocus conditions. The simulation parameters are: WPOA, C1, L1 and A0 (see Table 1 for definitions).

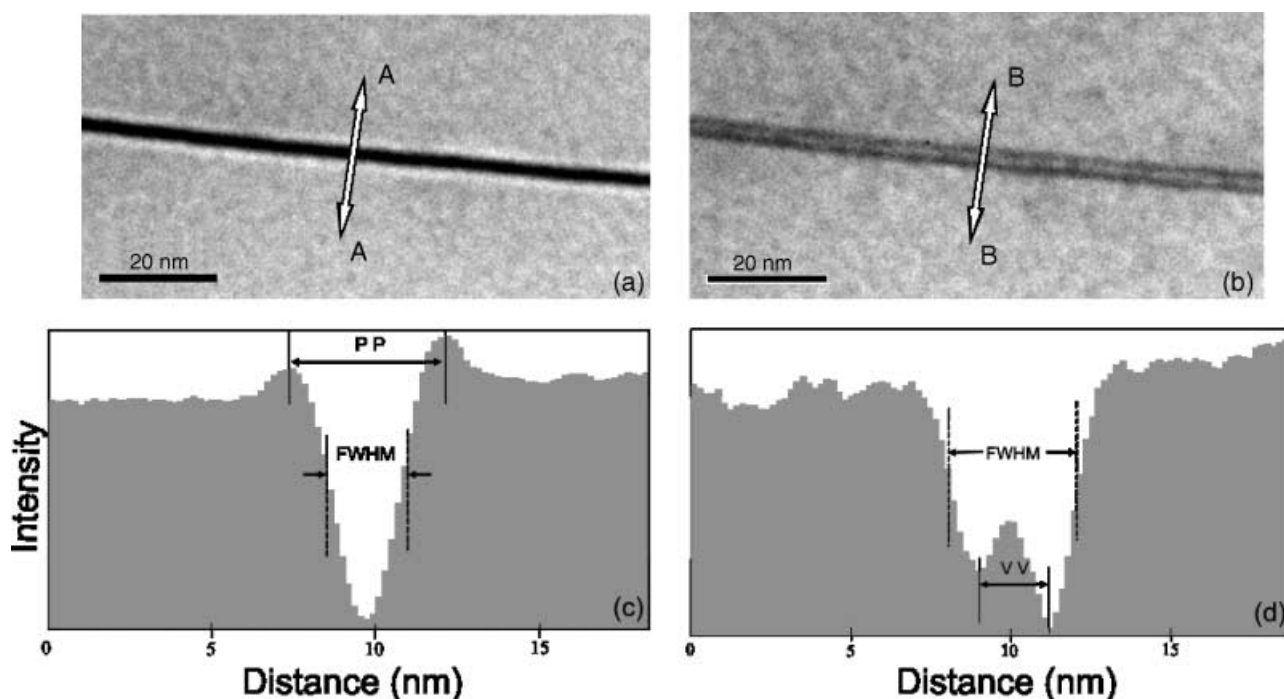


Fig. 6. Fresnel contrast images (FCIs) and profiles across the grain boundary of a  $\text{Si}_3\text{N}_4$  sample doped with Lu-Mg. (a) FCI at a defocus value of  $+1.2 \mu\text{m}$ ; (b) FCI at a defocus value of  $-1.2 \mu\text{m}$ ; (c) plot of profile across the line AA integrated over a width of  $18.8 \text{ nm}$ ; (d) profile across the line BB integrated over a width of  $18.8 \text{ nm}$ . FWHM, full width at half the maximum; VV, valley-to-valley.

of the Fresnel contrast (see also Materials and Methods). The simulated Fresnel intensity profiles at various defocus values are shown in Fig. 5(b)–(h). The Fresnel profiles corresponding to a defocus of  $\pm 2.2 \mu\text{m}$ , as presented in Fig. 5(h) (a schematic version of this figure is shown as fig. 1 in Ness

*et al.*, 1986), show two features: (i) left–right mirror symmetry (LR symmetry); (ii) inversion symmetry across the  $x$ -axis between overfocus and underfocus profiles (OU symmetry).

Figure 6(a,b) shows experimental FCIs of the  $\text{Si}_3\text{N}_4$  sample taken by a Zeiss-912 microscope at a defocus of  $+1.2$  and  $-1.2$

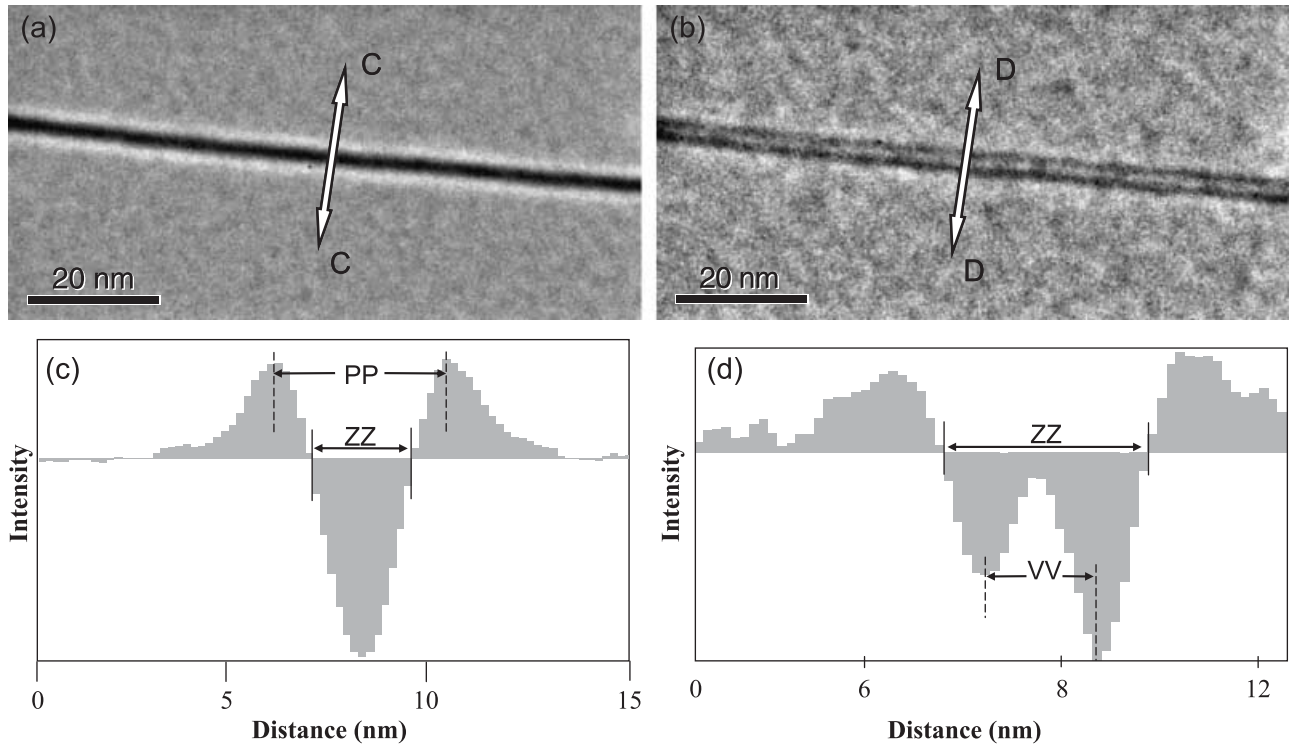


Fig. 7. Fourier-filtered-Fresnel contrast images and profiles across the grain boundary. (a) Image obtained from Fig. 6(a) by Fourier filtering the central spot; (b) image obtained from Fig. 6(b) by Fourier filtering the central spot; (c) profile across the line CC integrated over a width of 18.8 nm; (d) profile across the line DD integrated over a width of 18.8 nm.

$\mu\text{m}$ , respectively. Figure 6(c,d) shows the corresponding intensity profiles across the IGF integrated over a width of 18.8 nm along the interface. Figure 7(a–b) was obtained by filtering out the central spot from the Fourier transformation of Fig 6(a,b), respectively, using mask M3. Figure 7(c–d) shows the intensity profiles across Fig. 7(a,b), respectively. The various distances measured [peak-to-peak (PP), FWHM, zero-to-zero (ZZ) and valley-to-valley (VV)] are also illustrated in Figs 6 and 7. The following points can be observed from the figures:

- (i) in overfocus (Fig. 6c), the background intensity level from the grains on either side of the GB is different but the peak intensities are seen to be equal (Fig. 7c),
- (ii) in underfocus (Fig. 6b), the intensity of the valleys are not equal for an identical value of defocus (Fig. 7d),
- (iii) PP distance measured from Fig. 6(c) (+1.2  $\mu\text{m}$ , overfocus) is not equal to the VV distance measured from Fig. 6(d) (–1.2  $\mu\text{m}$ , underfocus).

Hence, it is seen that LR and OU symmetries are broken in the experimental FCIs. This symmetry breaking may happen due to the shape of the potential profile across the IGF or because of the effect of specimen thickness along the direction of the electron beam. To understand the effect of various potential profiles and specimen thicknesses along the electron beam, different cases are considered, as listed in Table 3. The profile

P3 is chosen to reflect segregation of a dopant with a scattering potential higher than the grains adjacent to the IGF. Parameters used in the simulation are listed in Table 1. The important points which can be seen from this table are:

- (i) under the weak-phase-object approximation (WPOA), i.e. for very thin specimens, LR symmetry and approximate OU symmetry are present (for profile P1);
- (ii) in the Fresnel profiles generated using the phase-object approximation (POA), the OU symmetry is broken (P1);
- (iii) LR asymmetry in the potential profile leads to a LR asymmetry in the Fresnel profiles (profiles P2 and P3), however, approximate OU symmetry is maintained.

In the standard Fresnel fringe extrapolation technique, a plot of fringe spacing ( $s$ ) versus the square root of defocus ( $(\Delta f)^{1/2}$ ) is extrapolated to zero-defocus to obtain the thickness of the IGF. Figure 8 shows the plot of  $s$  (measured from Fig. 5b–h) versus  $(\Delta f)^{1/2}$  obtained from simulation using a square-well potential (Fig. 5a). The following points are noted from the simulation (Figs 5 and 8):

- (i) at large defocus values ( $|(\Delta f)| > 1.6 \mu\text{m}$ ) there are prominent primary fringes;
- (ii) at low defocus values ( $|(\Delta f)| < 1.4 \mu\text{m}$ ) the intensities of the primary and secondary fringes are comparable (furthermore it is observed that, the peak of the primary fringe is not distinct below  $|(\Delta f)| < 0.8 \mu\text{m}$ );

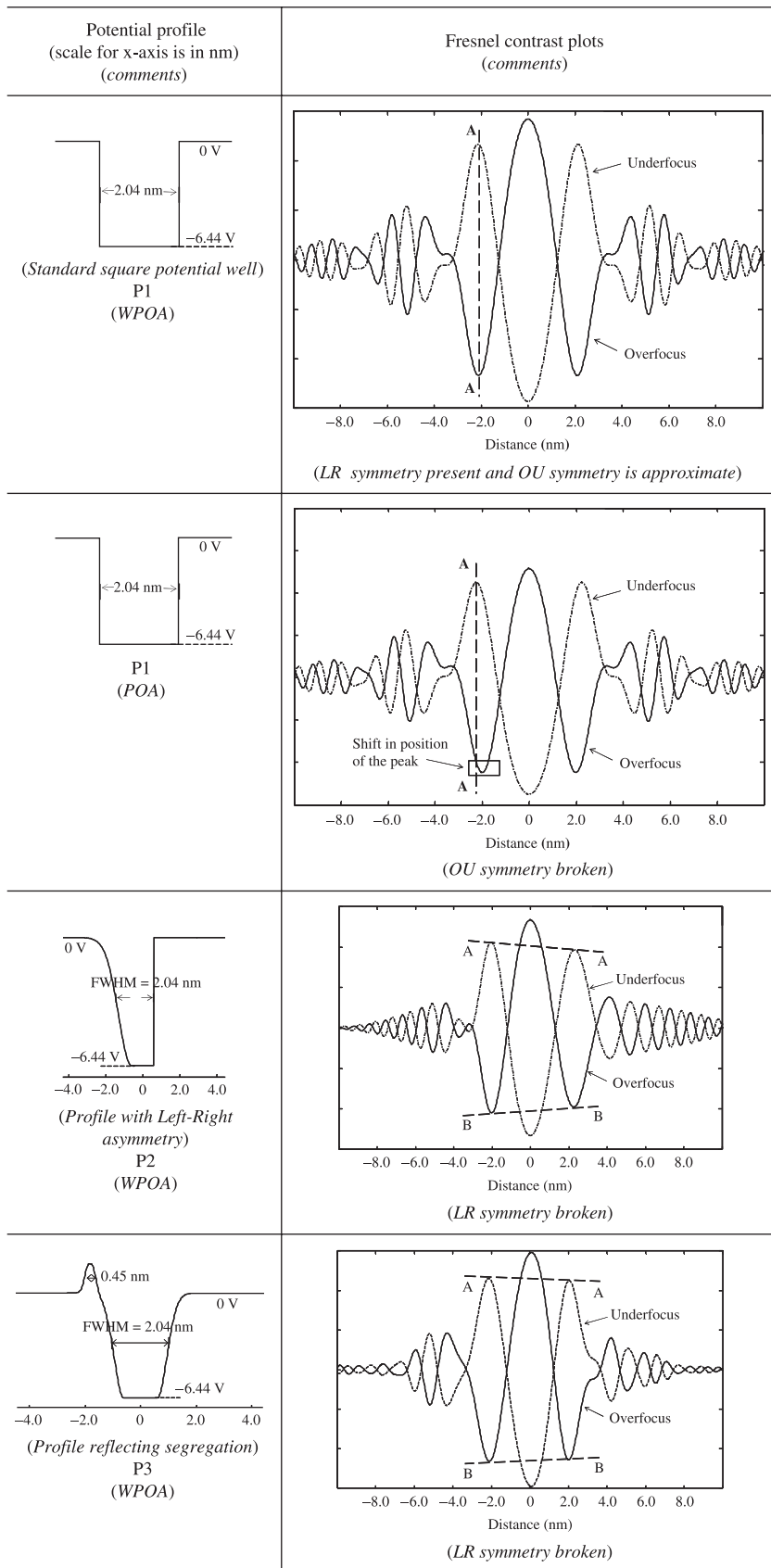


**Table 3.** Effect of various intergranular glassy film (IGF) potential profiles and assumptions of the Fresnel contrast image (FCI). WPOA, weak-phase-object approximation; Defocus =  $\pm 2.2 \mu\text{m}$ ,  $C_s = 2.7 \text{ mm}$ .

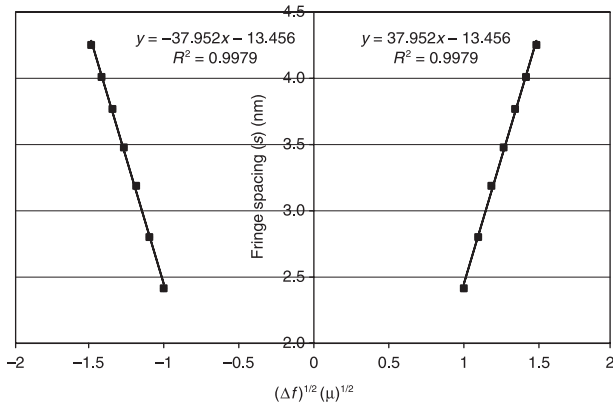


**Fig. 8.** Plot of fringe spacing ( $s$ ) versus square-root of the defocus  $(\Delta f)^{1/2}$  for a square-well potential (Fig. 5a). The fringe spacings are measured from Fig. 5(b–h). The simulation parameters are: WPAO, C1, L1 and A0 (see Table 1 for definitions).

- (iii) the linear fit in the plot of  $s$  versus  $(\Delta f)^{1/2}$  is not good for low defocus values ( $< 1 \mu\text{m}$ );
- (iv) extrapolation to zero-defocus does not give the correct thickness of the IGF (a negative value of  $-1.346 \text{ nm}$  is obtained). Instead, extrapolation to a defocus value where the 'primary' fringe is first visible (of  $\sim \Delta f = 0.8 \mu\text{m}$ ) gives a good estimate of the thickness of the IGF (of  $\sim 2.0 \text{ nm}$ )

An additional point to be noted is that, in an actual experiment with a microscope such as the Zeiss-912, the two peaks seen at an overfocus of  $1.2 \mu\text{m}$  (labelled m1 and m2 in Fig. 5c), would be seen as one peak at an average spacing between m1 and m2. Hence, at low underfocus values, the measurements from an experiment would be an overestimate. This in itself would lead to a nonlinear plot of fringe spacing versus  $(\Delta f)^{1/2}$ , even for a square potential profile.

### Measurement of thickness and comparison

#### Using Fresnel fringes hidden in high-resolution micrographs

To illustrate the utility of the Fresnel fringes hidden in HRMs, two cases are considered in this section. In the first case (Lu-Mg-doped  $\text{Si}_3\text{N}_4$ ), the lattice fringes on one side are nearly parallel to the GB and hence a plot of the intensity profile across the IGF shows oscillations due to lattice fringes superimposed on the Fresnel fringe contrast. The stoichiometric  $\text{SrTiO}_3$  sample is used to demonstrate the use of the method, when lattice fringes are very weak on one side of the IGF.

*Case 1: Lu-Mg-doped  $\text{Si}_3\text{N}_4$ .* Figure 9(a) shows the standard method of measurement of the thickness of an IGF from lattice fringe images in a HRM (HRT), taken at an overfocus of  $40 \text{ nm}$ . Figure 9(b) shows the use of Fourier-filtered-HRMs (FF-HRMs)

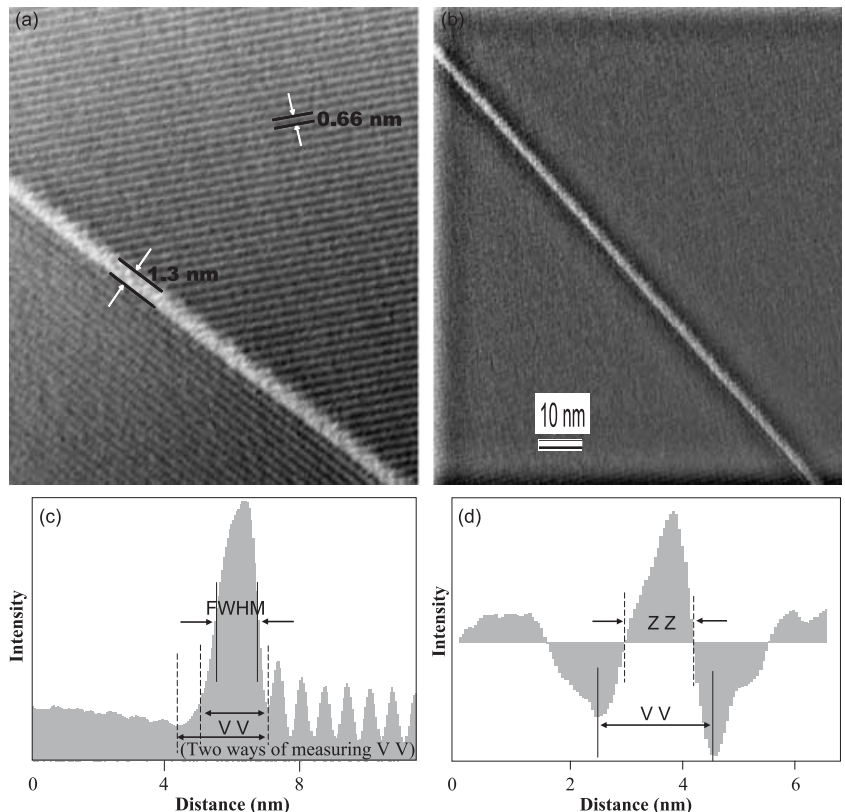


**Fig. 9.** Use of high-resolution micrographs (HRMs) for the measurement of the thickness of an intergranular glassy film in a Lu-Mg-doped  $\text{Si}_3\text{N}_4$  sample. (a) HRM; (b) Fourier-filtered (FF)-HRM; (c) profile across the grain boundary (GB) in the HRM integrated over a width of  $4.4 \text{ nm}$ ; (d) profile across the GB in the FF-HRM (integrated over a width of  $8.8 \text{ nm}$ ). FWHM, full width at half the maximum; VV, valley-to-valley; ZZ, zero-to-zero.

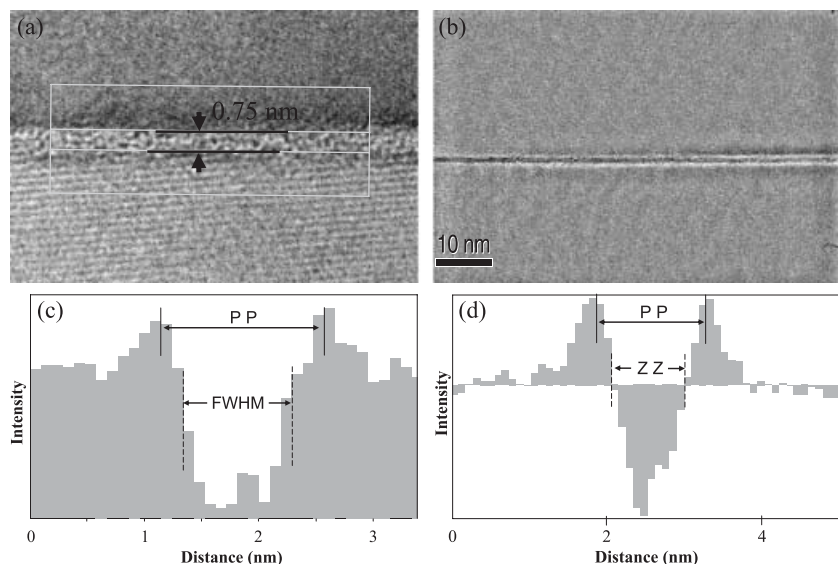


**Fig. 10.** Measurement of the thickness of an intergranular glassy film (IGF) in the stoichiometric  $\text{SrTiO}_3$  (STO1). (a) High-resolution micrograph (HRM); (b) Fourier-filtered (FF)-HRM; (c) profile across the grain boundary (GB) in the HRM; (d) profile across the GB in the FF-HRM. Note that the lattice fringes are weak on one side of the IGF. FWHM, full width at half the maximum; PP, peak-to-peak; ZZ, zero-to-zero.

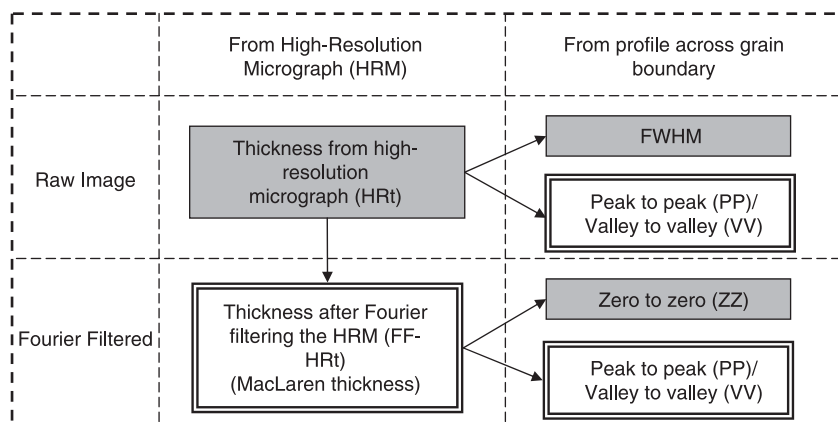


**Fig. 11.** Schematic diagram showing the measurement of thickness from a high-resolution micrograph (HRM). Thickness can be calculated directly from the HRM (HRT) or by Fourier filtering the lattice fringes from the micrograph (FF-HRT). An easier alternative is to use the plot of profiles across these images. Values which correlate with each other are shown either by the same shading or by the same border.

for the same procedure (mask size M3). The use of FF-HRMs corresponds to the technique of MacLaren (2004) and the thickness measured is henceforth referred to as the MacLaren thickness. Figure 9(c) shows the intensity profile across the IGF (from Fig. 9a), integrated over a width of 4.4 nm, showing the hidden Fresnel fringe contrast. Figure 9(c) also shows two distances which can be calculated from the profile: the FWHM and the VV distance. Figure 9(d) shows the intensity profile across the IGF from the Fourier-filtered image (Fig. 9b). Figure 9(d) also shows two ways of determining the thickness of the IGF based on the Fourier-filtered image: the ZZ distance and VV distance.

**Case 2: stoichiometric  $\text{SrTiO}_3$ .** Figure 10 is in an identical format to Fig. 9, but is taken from a grain boundary of the  $\text{SrTiO}_3$  ceramic at an underfocus of 40 nm. It is seen that lattice fringes are very weak on one side of the IGF and hence a clear demarcation of the crystal–glass interface on that side is not possible from the HRM alone. Figure 10(c) shows that there is no superimposition of high-resolution fringes with Fresnel

fringes, which leads to a straightforward measurement of the peak to peak spacing.

**Comparison of the thicknesses measured.** The essence of the methodology adopted above is illustrated in Fig. 11, which shows the measurement of thickness of an IGF in four different ways. A comparison of the thicknesses measured in earlier sub-sections is shown in Table 4. It is seen that the VV/PP distance measured from the profiles (raw and Fourier-filtered data) correlates well with the thickness calculated using the MacLaren technique and that the FWHM (from the profile of the raw data) and ZZ (from the profile of the Fourier-filtered data) distances correspond well with the HRT.

### Use of conventional Fresnel fringes

#### Extrapolation of Fourier-filtered Fresnel fringe spacing data

Table 5 shows a compilation of the distances measured from Figs 6 and 7, obtained at defocus values of  $\pm 1.2 \mu\text{m}$  from the

**Fig. 12.** Schematic diagram showing the use of Fresnel fringe spacing data for the calculation of the thickness of an intergranular glassy film. Raw and Fourier-filtered images are considered for under and overfocus conditions. Spacings which correspond to each other have the same shading or the same borders. Correlations between underfocus and overfocus fringe spacings are shown by similar but different shading or borders. FWHM, full width at half the maximum.

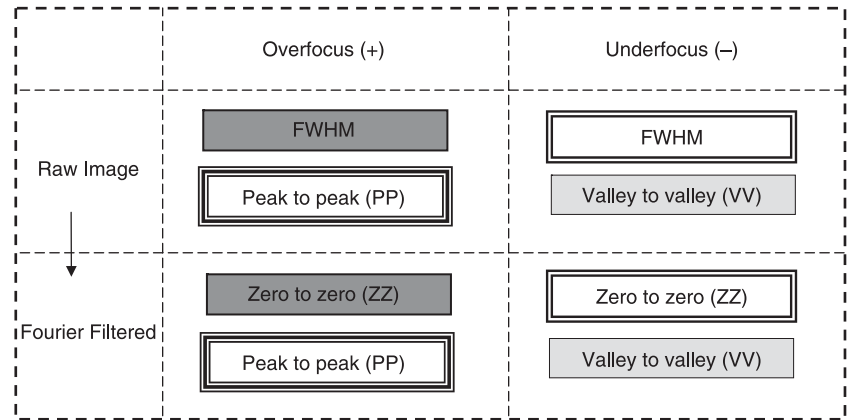


**Table 4.** A comparison of the values of thickness obtained from high-resolution micrographs (HRts) and from the plot of intensity profiles across the intergranular glassy film revealing Fresnel fringes. Additionally, the high-resolution image is Fourier-filtered (FF) to obtain the MacLaren thickness (FF-HRt) and the FF Fresnel thickness (FF-Ft); as measured from the intensity profile across the FF image. Correspondences are shown, either by similar shading, similar border or by similar font.

Sample (Lattice fringe orientation)	HRt (nm)	FF-HRt (Maclaren thickness) (nm)	From intensity (Fresnel) profiles			
			Ft (nm)		FF-Ft (nm)	
			FWHM	PP/VV	Z-Z	PP/VV
Lu-doped Si <sub>3</sub> N <sub>4</sub> (parallel to GB on one side)	1.18	1.95	1.18	1.98–2.6 <sup>a</sup>	1.18	1.98
Stoichiometric SrTiO <sub>3</sub> (STO1) (not parallel to GB on either side)	0.95	1.51	0.95	1.53	0.94	1.51

<sup>a</sup>Depending on the choice of the VV distance.

**Table 5.** A comparison of the fringe spacing values obtained from profiles across under and overfocus FCI taken at a defocus value of  $\pm 1.2 \mu\text{m}$ .

Condition	Fresnel data (nm)		Fourier filtered Fresnel data (nm)	
	FWHM	PP/VV	ZZ	PP/VV
Overfocus (+)	2.26	4.14	2.45	4.33
Underfocus (-)	3.77	2.07	3.96	2.07

FWHM, PP, VV and ZZ are illustrated in Figs 6 and 7.

Si<sub>3</sub>N<sub>4</sub> sample. The microscopy was performed on a Zeiss-912 machine, using the in-column energy filter. It is seen that the measured FWHM from the FCI correlates well with the ZZ distance from the FF-FCI and that the PP/VV distance from the FCI is similar to that from the FF-FCI. These correlations are illustrated schematically in Fig. 12.

The difficulties associated with the standard Fresnel fringe extrapolation technique and possible ways to overcome these are discussed here. The plot of the Fresnel fringe spacing data for the two methods (i.e. from the raw image and from the Fourier-filtered image) of measuring the fringe spacing are shown in Fig. 13. The data are extrapolated to the zero-defocus value to obtain the thickness of the IGF by: (a) the standard method (dashed line) and; (b) the data obtained by FF-FCI (solid line). The thickness of the IGF (from Fig. 13) by the standard method is  $\sim 0$  nm whereas the thickness calculated from the Fourier-filtered images is 0.9 nm. It is clearly seen that the Fourier filtering method gives an estimate closer to the value obtained by a HRM (1.3 nm) than the standard method.

Figure 14(a) shows the plot of the data from FF-FCI (FF-ZZ) obtained from a GB containing an IGF from the nonstoichiometric SrTiO<sub>3</sub> sample (STO2). The microscopy was performed on a JEOL 4000EX microscope. The figure shows a plot of FF-ZZ versus the root of defocus ( $(\Delta f)^{1/2}$ ). Due to noisy images close to zero-defocus, the measurement of the PP distance is

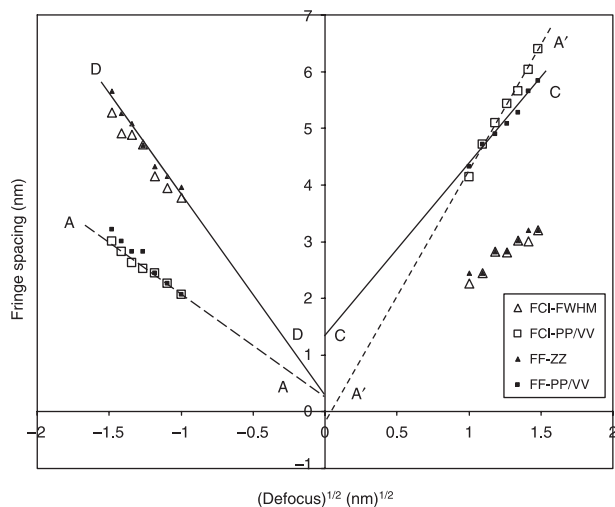


**Fig. 13.** Plot of the fringe spacing data obtained from a Fresnel contrast image (FCI) and a Fourier-filtered (FF)-FCI (Lu-Mg-doped  $\text{Si}_3\text{N}_4$  sample). The distances plotted are: FCI peak-to-peak/valley-to-valley (PP/VV), FCI full width at half the maximum (FWHM), FF-FCI PP/VV and FF-FCI zero-to-zero (ZZ). Lines AA and A'A' are the extrapolation of the data of FCI PP/VV and underfocus data in FF-FCI ZZ. Each data point is associated with an error bar of  $\pm 0.2$  nm (not plotted for clarity). The thickness of the intergranular glassy film is obtained by extrapolating the lines to zero-defocus.

prone to error and hence the ZZ distance is chosen for the plot (e.g. Fig. 14b shows the profile across a FF-FCI taken at a defocus of  $-10$  nm). Additionally, due to the bent boundaries (unlike the  $\text{Si}_3\text{N}_4$  sample, Fig. 14c), integration over long distances along the IGF (to reduce noise), is not possible. It is seen that close to zero-defocus ( $= \pm 40$  nm) the plot of  $s$  versus  $(\Delta f)^{1/2}$  is not linear. However, at larger defocus values the curve is linear. The regions of linearity are marked in the Fig. 14(a). One of the reasons for the overestimate of the spacing at low defocus values compared with a linear plot could be the same

as the one mentioned in the Potential profiles and Fresnel contrast section (i.e. the primary and secondary peaks in the FCI, could be seen as one peak with an average spacing).

### Zero-defocus images

As in the case of the Fresnel fringes hidden in HRMs, the zero-defocus images can also be used for the measurement of the thickness of an IGF. Figure 15(a) shows the FF-FCI obtained from an image taken at zero-defocus from the  $\text{Si}_3\text{N}_4$  sample. Figure 15b shows the profile across the IGF integrated over a width of 12.4 nm. The thickness measured from the profile (the ZZ distance) is 1.2 nm which correlates well with the HRt of 1.2 nm. This method of zero-defocus imaging applied to a GB in the STO2 sample gives the thickness of the IGF as 1.2 nm (Fig. 14a). The thickness measured from the HRM (Fig. 14c) is about 1.0 nm. Only an approximate value could be obtained from the HRM due to the bent nature of the GB and local variations in the thickness. Figure 16 illustrates the utility of zero-defocus images for the case of a dry boundary (zero thickness). Figure 16(a) shows the HRM and Fig. 16(b) shows the intensity profile across the FF-FCI. It is to be noted that the accuracy of determination of the thickness from a zero-defocus image is dependent on the accuracy with which the zero-defocus is set. FF-FCI comes to the aid here too and a practical approach would be to determine the minimum thickness from a series of images (FF-FCI) near expected zero-defocus. The zero-defocus condition can be chosen from the series of images, corresponding to the image at the minimum thickness measured, or in the middle of a range of defocus values where the thickness is nearly constant.

### Discussion

#### Fourier filtering of high-resolution micrographs

Due to microscope- or material-imposed constraints, it is sometimes not possible to obtain lattice fringes from both sides of an

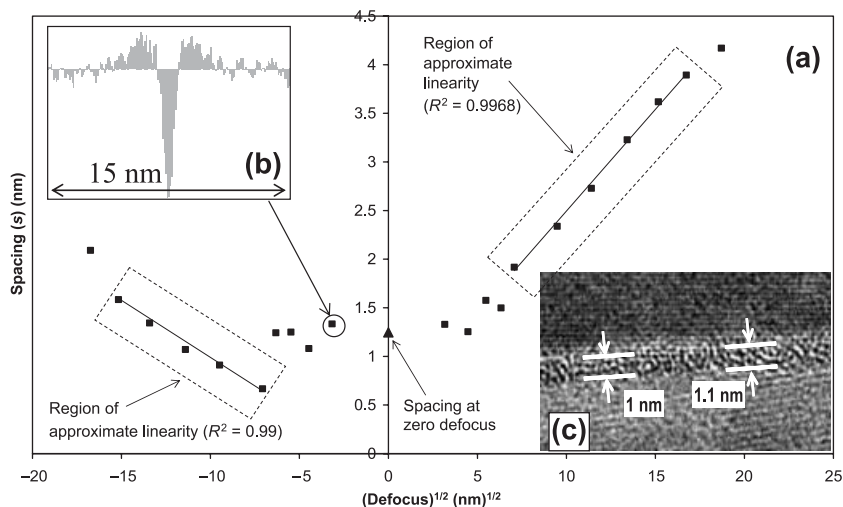


**Fig. 14.** Fourier-filtered-Fresnel contrast image zero-to-zero data obtained from a grain boundary containing an intergranular glassy film from the nonstoichiometric  $\text{SrTiO}_3$  (STO2) sample. (a) Plot of the spacing ( $s$ ) versus the root of defocus ( $(\Delta f)^{1/2}$ ); (b) profile across an image taken at an underfocus of 10 nm, integrated over a width of 12.4 nm; (c) HRM at an underfocus of 10 nm.

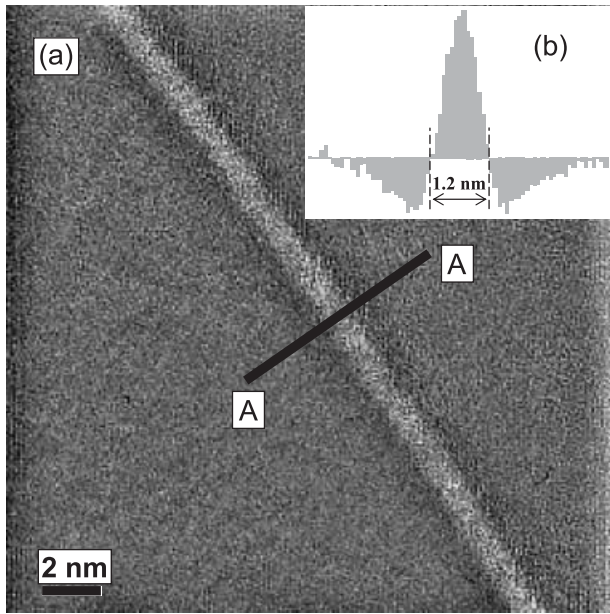


Fig. 15. Utility of zero-defocus Fourier-filtered-Fresnel contrast image (FF-FCI) in measuring the thickness of the intergranular glassy film from the  $\text{Si}_3\text{N}_4$  sample. (a) FF-FCI; (b) plot of the profile across the line AA integrated over a width of 12.4 nm.

IGF. Previously such a HRM would be considered useless for the measurement of the thickness of an IGF. Using profiles across the FF-HRM the utility of such images can be enhanced and thickness of the IGF can be measured (as shown in Figs 9 and 10).

It is seen that the procedure developed here yields good results for two samples of vastly different natures ( $\text{Si}_3\text{N}_4$  and  $\text{SrTiO}_3$ ). The  $\text{Si}_3\text{N}_4$  sample has mainly faceted grains (implying straight GBs) with sizes in the region of tens of nanometres and almost all the GBs have IGFs. By contrast, the  $\text{SrTiO}_3$  sample has grain sizes of about  $50 \mu\text{m}$  with curved GBs. Additionally, most of the GBs in the stoichiometric  $\text{SrTiO}_3$  sample are dry (Subramaniam *et al.* to be communicated). Furthermore, different microscopes and defocus values were chosen to test the applicability of the method under a wider range of conditions. High-resolution microscopy on the  $\text{Si}_3\text{N}_4$  sample was carried out with a JEOL 4000FX microscope (with a point-to-point resolution of 0.2 nm) and an overfocus value of 40 nm was used for imaging. Microscopy on the  $\text{SrTiO}_3$  samples was performed with a JEOL 4000EX (with a point-to-point resolution of 1.8 nm) at an underfocus of 40 nm.

#### Extrapolation of fringe spacing data for measuring IGF thickness

The technique of extrapolation of Fresnel fringe spacing data has proved to be a useful tool for the measurement of the thickness of IGFs. Unfortunately the Fresnel contrast obtained from many GBs is poor. Additionally, there could be considerable scatter in the fringe spacing data, leading to a reduced accuracy

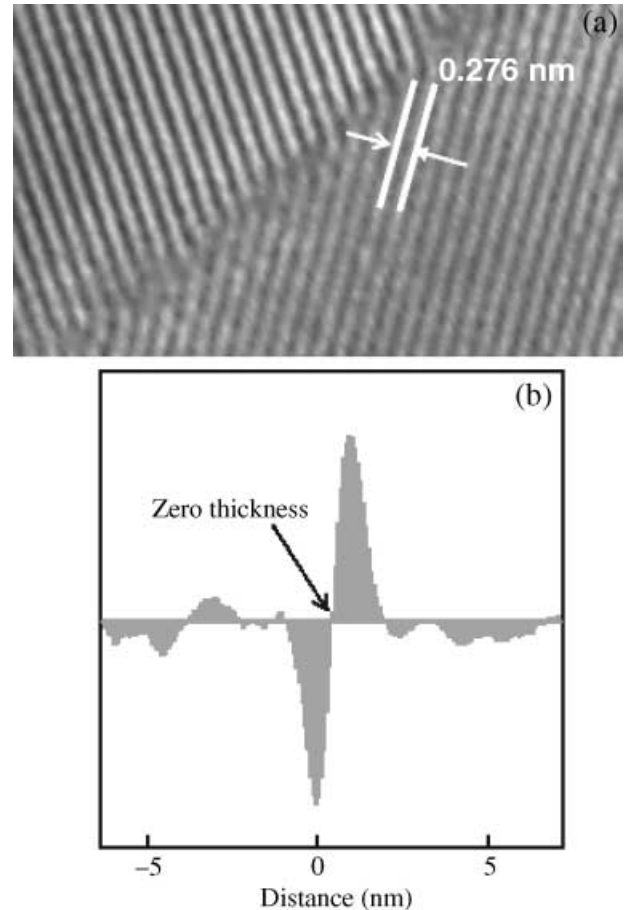


Fig. 16. Illustrative case for the use of zero-defocus images from a dry grain boundary in  $\text{SrTiO}_3$  (STO1). (a) High-resolution micrograph; (b) profile across the Fourier-filtered-Fresnel contrast image showing zero thickness.

of the extrapolation. Determination of zero-defocus using Fresnel contrast has also proven tricky. These problems are further compounded in the case of diffuse interfaces as the model for extrapolation is based on a square-well potential (linear plot of spacing versus  $(\Delta f)^{1/2}$ ). The presence of these issues is encountered even during the present investigation.

From the simulated Fresnel profiles in the current work (Fig. 8) and Rasmussen & Carter (1990) (fig. 6, Model A in that paper replotted here as Fig. 17), it is seen that the linearity in the plot of  $s$  versus  $(\Delta f)^{1/2}$  is valid in certain regions only. Furthermore, extrapolation of the fringe spacing data does not lead to the correct value of thickness. From simulation of Fresnel intensity profiles, it is seen that both LR and OU symmetries, present in an ideal (using WPOA) Fresnel profile can be broken; as seen in the results of the simulations (Table 3). However, due to the limitations of an 1D potential profile, different kinds of profiles can lead to similar features in Fresnel contrast and hence, it is not possible to separate some of the structural effects causing the asymmetry in the potential profile.

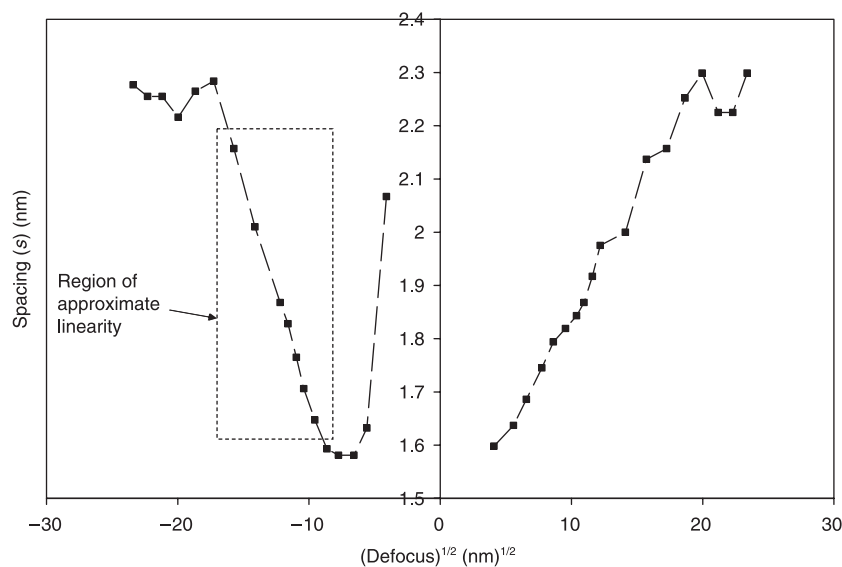


Fig. 17. Replot of data from Rasmussen & Carter (1990) (Fig. 6, Model A in Rasmussen & Carter) showing left–right asymmetry and regions of validity of linear  $s$  versus  $(\Delta f)^{1/2}$ .

In the current work (Lu-Mg-doped  $\text{Si}_3\text{N}_4$  sample) it is seen that some objectivity can be introduced into the calculations based on Fresnel fringe images. Instead of using the VV distance in underfocused images, use of the FWHM distance (Fig. 6) results in better symmetry between underfocus and overfocus data plots. It is seen that measurement of the ZZ distance in the FF-FCI (Fig. 7) is easier than measuring the FWHM. The reason for the restoration of symmetry by this procedure is not clear at this point, but in light of the presented simulations it is satisfactory that a reasonable value for the thickness of the IGF can be obtained by this method. However, given the limited validity of the extrapolation technique, it is rather surprising that the method works, albeit with limited precision. The reasons for the good results obtained by previous researchers using the extrapolation technique on  $\text{Si}_3\text{N}_4$  samples of different compositions [(i)  $\text{Y}_2\text{O}_3 + \text{MgO}$ -doped  $\text{Si}_3\text{N}_4$  (Cinibulk *et al.*, 1993); (ii) high-purity  $\text{Si}_3\text{N}_4$  (Jin *et al.*, 1998)], are also not understood in the light of the current research. It is to be noted that the earlier researchers, instead of plotting  $s$  versus  $(\Delta f)^{1/2}$ , plotted  $s$  versus  $\Delta f$  and had used this nonlinear plot for extrapolation. A plot of  $s$  versus  $(\Delta f)^{1/2}$  is better for visualization of the trends, especially in the linear regimes.

#### Fourier filtering of zero-defocus images

Fourier filtering of standard FCIs enhances the contrast of an image. The zero-defocus value can be accurately set by using FF-FCI, as contrast is very poor under these low defocus conditions (Fig. 14). This enhancement in contrast also allows us to extend the useful range of defocus values from which fringe spacing data can be obtained. The thickness measured from zero-defocus FF-FCI is in good correspondence with that measured from a HRM; the reason for which can be understood by simulating the 1D intensity profiles from potential profiles across the IGF. This neatly ties back in with the utility

of the hidden Fresnel fringes in HRMs for thickness measurement. As is apparent, the resolution of the microscope needs to be high for ideal correspondence.

#### Different measurements of IGF thickness

Two IGF thicknesses were calculated by MacLaren (2004) (HRM and FF-HRM). Using the current method it is seen that these values can be correlated well with the values obtained from hidden Fresnel fringes. The question as to where the boundary between the glass and the crystal should be drawn has remained somewhat arbitrary so far. Using hidden Fresnel fringes this issue can be objectively addressed and the measurement can be made more rigorous by using the ZZ distance of the intensity profile across the IGF in an FF-HRM (especially if there are local variations in thickness). A direct correlation is seen between the thicknesses obtained from an HRM (HRT and FF-HRT) and the thicknesses measured using hidden Fresnel fringes (Table 4 and Fig. 9). The reason for this correlation can be understood from the simulations shown in Fig. 4(c and e). As the HRMs (Figs 9a and 10a) are taken at low defocus values, the FWHM of the boundary width captured in the FF-HRM, is not much different from the true width that would be measured from a zero-defocus image. It is to be noted that (as also seen in Fig. 14), the Fresnel fringe spacing (ZZ) is an insensitive function of the defocus at low defocus values. Hence, the error introduced by imaging at low defocus values (as in the case of hidden Fresnel fringes in the high-resolution microscope) is small. However, under ideal conditions zero-defocus should be used.

For other material/microscope combinations, the microscopic parameters (defocus values, size of the objective aperture, etc.) which give such correlations may have to be worked out.

In this context it should be noted that the HRT is usually thought to be representative of the core of the IGF (the width 'a' in Fig. 2a), i.e. it captures the part of the IGF with close to

100% amorphicity (Fig. 3a). As the HRT is equal to the ZZ distance in the zero-defocus FF-FCI, which in turn is a measure of the FWHM of the potential profile (simulations: Figs 2a and 4e); the HRT corresponds to the FWHM of the potential profile and not the inner width 'a'. Another way of interpreting the result would be to conclude that the IGF has no 'core' region and is fully diffuse (i.e. the diffuse profiles overlap). A note of caution here would be that the FWHM could over- or under-represent the width, depending upon the shape of the potential profile (especially for very peculiarly shaped profiles), and the correlations seen above can be assumed to be valid for 'reasonably shaped' potential profiles. As the MacLaren thickness is always greater than the HRT, so, it might correspond to the outer width of the potential profile (distance  $a_0$  in Fig. 2a) across the IGF.

#### Mask size needed for Fourier filtering

The optimum size of the mask used in Fourier filtering has been determined by calculations using a potential profile representing a diffuse interface. Real crystal-glass interfaces could have far more complicated profiles, especially in the presence of rare-earth additives to the ceramic, which could segregate to the interface. Additionally, the two interfaces could be different, breaking the symmetry assumed in an ideal mathematical model. Our calculations show that the size of the mask is very important, as was to be expected. However, a change of 20–30% in mask size does not significantly affect the values measured from the Fourier-filtered image. A simple rule of thumb can be derived from the calculations based on the ideal profile. These show that a mask of size of  $0.2/a_{\text{FWHM}}$  to  $0.3/a_{\text{FWHM}}$  ( $a_{\text{FWHM}}$  is the FWHM of the GB potential profile) gives good results.

Finally, it should be noted that the procedures described here may not be useful/needed for certain materials/microscopes.

#### Conclusions

- (i) The utility of Fresnel contrast and high-resolution images can be enhanced by Fourier filtering the images. This methodology, applied to high-resolution micrographs, allows the use of images in which lattice fringes are weak (or even absent) on one side of the IGF and in the case of FCIs gives better interpretability from noisy images.
- (ii) A simple new technique is proposed, wherein Fresnel contrast hidden in high-resolution images is used to objectively demarcate the glass-crystal interface and to measure the thickness of an IGF (by Fourier filtering the lattice fringes). The optimum mask size was determined by simulations on 1D scattering potential profiles.
- (iii) Experimental results (on  $\text{Si}_3\text{N}_4$  doped with Lu-Mg and stoichiometric and nonstoichiometric  $\text{SrTiO}_3$ ) and simulations show that the plot of fringe spacing ( $s$ ) versus root of defocus ( $(\Delta f)^{1/2}$ ) is not linear over the entire defocus

range but only at intermediate defocus values. Other limitations of the Fresnel extrapolation technique are also detailed, including the important observation that the correct thickness of the IGF is not obtained by this method.

- (iv) A new method is developed wherein Fresnel fringe spacing is measured based on Fourier filtered Fresnel images. Appropriate choice of spacing values from over- and underfocus images is seen to give a better symmetry in plots of Fresnel fringe spacing data. It is also seen that this technique gives a better estimate of the thickness of the IGF from the same set of FCIs by extrapolation to zero-defocus. The approximate validity of the extrapolation method could not be determined in the framework of the simulations performed.
- (v) Simulations of Fresnel contrast using 1D potential profiles were used for understanding the different sources of LR and OU symmetry breaking being observed in experimental FCIs.
- (vi) In light of the limitations of the Fresnel extrapolation method, a new technique for the measurement of the thickness of IGFs based on Fourier-filtered zero-defocus images was tested on  $\text{Si}_3\text{N}_4$  doped with Lu-Mg and nonstoichiometric  $\text{SrTiO}_3$  samples. This has been found to be the simplest technique for the purpose of estimating the high-resolution thickness without actually performing lattice fringe imaging. Simulations are used to validate the method.
- (vii) Thickness measured from lattice fringe imaging (HRT) is equal to the ZZ distance in the zero-defocus FF-FCI (hidden in HRMs or otherwise), which in turn is a measure of the FWHM of the potential profile (as seen in simulations). This implies: (a) the HRT corresponds to the FWHM of the potential profile and not the inner width ('a') or (b) the IGF is fully diffuse. The current work is not able to differentiate between the two cases. The measure of IGF thickness used by MacLaren (2004) might be the outer width of the potential profile across the IGF.

#### Acknowledgements

The financial assistance from the European Commission under contract Nr. G5RD-CT-2001-00586 (NANOAM) is acknowledged. Anandh Subramaniam wishes to acknowledge the Alexander von Humboldt foundation for their research fellowship. The authors are thankful to Dr Raphaele Satet and Prof. Michael Hoffmann (University of Karlsruhe) for providing the samples used in the work. Heartfelt thanks are expressed for Ute Salzberger, Marion Kelsch, Peter Kopold and Kersten Hahn for their consistent support.

#### References

- Ackler, H.D. (1997) *Thermodynamic calculations and model experiments on thin intergranular amorphous films in ceramics*. PhD Thesis, Massachusetts Institute of Technology, Boston.

- Bhattacharyya, S., Koch, C.T. & Rühle, M. (2006) Projected potential profiles across interfaces obtained by reconstructing the exit face wave function from through focal series. *Ultramicrosc.* In press.
- Bobeth, M., Clarke, D.R. & Pompe, W. (1999) A Diffuse Interface Description of Intergranular Films in Polycrystalline Ceramics. *J. Am. Ceram. Soc.* **82**, 1537–1546.
- Cinibulk, M.K., Kleebe, H.-J. & Rühle, M. (1993) Quantitative comparison of TEM techniques for determining amorphous intergranular film thickness. *J. Am. Ceram. Soc.* **76**, 426–432.
- Clarke, D.R. (1979) On the detection of thin intergranular films by electron microscopy. *Ultramicrosc.* **4**, 33–44.
- Döblinger, M., Cockayne, D.J.H., Meyer, R.R., Kirkland, A.I. & Manh, D.N. (2004) Induced order in intergranular films in  $\text{Si}_3\text{N}_4$ . *Proceedings of the 13th European Microscopy Congress*. Vol. II (ed. by D. Schryvers & J.-P. Timmermans), pp. 59–60. Belgian Society for Microscopy, Liège.
- Dunin-Borkowski, R.E. (2000) The development of Fresnel contrast analysis, and the interpretation of mean inner potential profiles at interfaces. *Ultramicrosc.* **83**, 193–216.
- Eöfving, M. & Olsson, E. (2002) Electron holography study of active interfaces in zinc oxide varistor materials. *J. Appl. Phys.* **92**, 5272–5280.
- Jin, Q., Wilkinson, D.S. & Weatherly, G.C. (1998) Determination of grain boundary film thickness by the Fresnel fringe imaging technique. *J. Eur. Ceram. Soc.* **18**, 2281–2286.
- Kleebe, H.-J. (1992)  $\text{SiC}$  and  $\text{Si}_3\text{N}_4$  materials with improved fracture resistance. *J. Eur. Ceram. Soc.* **10**, 151–159.
- Kleebe, H.-J. (1997) Structure and chemistry of interfaces in  $\text{Si}_3\text{N}_4$  materials studied by transmission electron microscopy. *J. Ceram. Soc. Jpn.* **105**, 453–475.
- Koch, C.T., Bhattacharyya, S., Subramaniam, A. & Rühle, M. (2004) Assessing thermodynamic properties of amorphous nanostructures by energy filtered electron diffraction. *Microsc. Microanal.* **10** (Suppl.), 254–255.
- Koch, C.T., Bhattacharyya, S., Rühle, M., Satet, R.L. & Hoffmann, M.J. (2005) Measuring electrostatic potential profiles across amorphous intergranular films by electron diffraction. *Microsc. Microanal.*, in press.
- Loudon, J.C., Lloyd, S.J., Midgley, P.A. & Mathur, N.D. (2001) The magnetic domain wall width of  $\text{La}_{0.7}\text{Ca}_{0.3}\text{MnO}_3$  determined from a Fresnel defocus series. *Inst Phys. Conf Ser.* **168**, 449–452.
- MacLaren, I. (2004) Imaging and thickness measurement of amorphous intergranular films using TEM. *Ultramicrosc.* **99**, 103–113.
- Ness, J.N., Stobbs, W.M. & Page, T.F. (1986) A TEM Fresnel diffraction-based method for characterizing thin grain boundary and interfacial films. *Phil. Mag. A*, **54**, 679–702.
- Peng, L.M. (1999) Electron atomic scattering factors and scattering potentials of crystals. *Micron*, **30**, 625–648.
- Rasmussen, D.R. & Carter, C.B. (1990) On the Fresnel-fringe technique for the analysis of interfacial films. *Ultramicrosc.* **32**, 337–348.
- Ross, F.M. & Stobbs, W.M. (1991) Computer modeling for Fresnel contrast analysis. *Phil. Mag. A*, **63**, 37–70.
- Satet, R.L. & Hoffmann, M.J. (2004) Impact of the intergranular film properties on microstructure and mechanical behaviour of silicon nitride. *Key Engg. Mater.* **264–268**, 775–780.
- Shibata, N., Pennycook, S.J., Gosnell, T.R., Painter, G.S., Shelton, W.A. & Becher, P.F. (2004) Observation of rare-earth segregation in silicon nitride ceramics at subnanometre dimensions. *Nature*, **428**, 730–733.
- Simpson, Y.K., Carter, C.B., Morrissey, K.J., Angelini, P. & Bentley, J. (1986) The identification of thin amorphous films at grain-boundaries in  $\text{Al}_2\text{O}_3$ . *J. Mat. Sci.* **21**, 2689–2696.
- Spence, J.C.H. (1981) *Experimental High-Resolution Electron Microscopy*. Clarendon Press, Oxford.
- Subramaniam, A., Šturm, S., Koch, C.T. & Rühle, M. Grain boundaries in stoichiometric polycrystalline  $\text{SrTiO}_3$ , to be communicated.
- Stobbs, W.M. & Ross, F.M. (1989) The Fresnel method for the characterization of interfaces. *Evaluation of Advanced Semiconductor Materials by Electron Microscopy*, NATO ASI Series B. Vol. 203 (ed. by D. Cherns), p. 183. Plenum Press, London.
- Wang, Y.G. & Dravid, V.P. (2002) Determination of electrostatic characteristics at a  $24^\circ$ , [001] tilt grain boundary in a  $\text{SrTiO}_3$  bicrystal by electron holography. *Phil. Mag. Lett.* **82**, 425–432.
- Williams, D.B. & Carter, C.B. (1996) *Transmission Electron Microscopy*, pp. 492–493. Plenum Press, New York.
- Winkelman, G.B., Dwyer, C., Hudson, T.S., et al. (2005) Three-dimensional organization of rare-earth atoms at grain boundaries in silicon nitride. *Appl. Phys. Lett.* **87**, Art. No. 061911.
- Ziegler, A., Idrobo, J.C., Cinibulk, M.K., Kisielowski, C., Browning, N.D. & Ritchie, R.O. (2004) Interface structure and atomic bonding characteristics in silicon nitride ceramics. *Science*, **306**, 1768–1770.